AIAA SciTech Forum
8-12 January 2024, Orlando, FL
AIAA SCITECH 2024 Forum

10.2514/6.2024-2148

Numerical study of transonic laminar shock buffet on the OALT25 airfoil

Hang Song*[1], Man Long Wong†[2], Aditya S. Ghate‡[2], and Sanjiva K. Lele§[1,2]
[1]*Department of Mechanical Engineering, Stanford University, Stanford, CA 94305, USA*
[2]*Department of Aeronautics & Astronautics, Stanford University, Stanford, CA 94305, USA*

A wall-resolved large-eddy simulation of a Mach 0.735 transonic flow over the OALT25 supercritical airfoil is performed using high-order compact finite difference schemes blended with a shock-capturing method to investigate the laminar shock buffet phenomenon. The airfoil is placed with an angle of attack of 4 deg., and the chord-length-based Reynolds number is one million. Data over a span of approximately 178 convective time units are used in the analysis. It is observed that the flow on the suction side remains laminar up to the separation region, and then transitions to turbulence. Large amplitude oscillation of the main shock occurs. Associated with the main shock buffet, periodic movement of the flow separation locations, formation and disappearance of a terminating shock, and turbulent vortex shedding are well captured in the simulation. The measurement shows that the shock buffet Strouhal number is approximately 0.1. The second dominant Strouhal number in the flow system is approximately 0.55, which is associated with turbulent vortex shedding. The variations of aerodynamic coefficients and signals of several flow properties measured at different probe locations are studied. Spectral proper orthogonal decomposition of different flow field variables is also conducted to further identify the correlation between the shock buffet and different flow phenomena.

I. Introduction

The shock oscillations over airfoils or wings in transonic flow is a critical issue in aeronautics [1, 2]. Shock unsteadiness, or shock buffet, can lead to strong structural vibrations and fluctuations of aerodynamic loads and moments, thus reducing the envelope of safe flight of an aerial vehicle. While transonic buffet has been studied for many decades, there is still a lack of full understanding of this shock instability phenomenon. Shock buffet in turbulent boundary layers, called turbulent buffet, has been widely studied both numerically and experimentally for a long period of time. Numerous experiments have been conducted using low-aspect ratio two-dimensional wings, or airfoils such as OAT15A [3], NACA0012 [4], RA16SC1 [5]. The turbulent buffet phenomena was also studied through numerical simulations such as Reynolds-averaged Navier–Stokes (RANS) simulations [6–8], hybrid RANS / large-eddy simulations (LES) [9–11], and wall-modeled large-eddy simulations (WMLES) [12–14].

In recent years, supercritical airfoils, or wings designed to generate extended laminar flow, are becoming more popular for the design of next-generation aircrafts [15], where low drag and high fuel efficiency are aimed for. Due to the emerging popularity of these laminar lifting devices, the study of laminar buffet, which involves the interaction of a laminar boundary layer with oscillating shocks, is becoming more critical. Unlike turbulent buffet that usually only involves a single oscillating shock on the suction side of an airfoil or wing, there can be multiple shocks involved in laminar buffet, and the shock structures can also be very complex [16]. To understand laminar transonic buffet, wind tunnel tests on laminar supercritical airfoils such as OALT25 designed by ONERA and V2C designed by Dassault Aviation were conducted under the BUTERFLI project [17] and the TFAST project [18, 19] respectively. In addition to wind tunnel tests, these problems were also studied with numerical simulations. Laminar buffet on the OALT25 airfoil configurations has been investigated in [20, 21] using LES, whereas the V2C airfoil was studied numerically with various simulation approaches [22–25]. For the OALT25 airfoil case, Dandois et al. [20] found higher frequency oscillations of the shock foot at the Strouhal number, St ≈ 1.2, from their simulations, in contrast to the lower shock buffet Strouhal number of St ≈ 0.07 observed in the experiments [17] at the same Reynolds number. Zauner et al. [21]

*Ph.D. Candidate, Department of Mechanical Engineering, Stanford University. AIAA Member. (songhang@stanford.edu)
†Ph.D. Alumni, Department of Aeronautics & Astronautics, Stanford University. AIAA Member. (wongml@stanford.edu)
‡Ph.D. Alumni, Department of Aeronautics & Astronautics, Stanford University. AIAA Member. (aditya90@stanford.edu)
§Edward C. Wells Professor, Department of Aeronautics & Astronautics and Department of Mechanical Engineering, Stanford University. AIAA Associated Fellow. (lele@stanford.edu)

conducted LES for transonic flows around the OALT25 airfoil at different Reynolds numbers and Mach numbers. They found a shock oscillation mode at the Strouhal number similar to the intermediate-frequency mode reported by Dandois et al. [20] but also another lower frequency mode. While this low-frequency mode has Strouhal number and mode shape similar to some previous studies on turbulent shock buffet [3, 9, 14, 26], it occurs under the conditions that the boundary layer upstream of the shock is laminar. These conditions are fundamentally different than the aforementioned works where the mode is usually suggested to be associated with fully turbulent boundary layers. Laminar buffet is still a newly discovered phenomenon and the underlying mechanism is relatively unexplored. The fact that the boundary layer is laminar before interacting with the shock foot requires well resolved solutions at direct numerical simulation (DNS) level near wall to reproduce the phenomenon in simulations. This is more challenging to study than turbulent buffet, especially at high Reynolds numbers of over 1 million for a laminar airfoil, as turbulent buffet can be studied using different turbulence approaches, such as RANS, hybrid RANS / LES, or WMLES, without the need to resolve the inner eddies of the boundary layers.

This work focuses on understanding the physical mechanisms that cause transonic, laminar shock buffet on a laminar supercritical airfoil. The study uses data generated from a wall-resolved LES of transonic flow over the OALT25 airfoil [17] at a Reynolds number of 1 million. The simulation details are provided in Sec. II. The simulation results and data analysis are shown in Sec. III. Finally, the conclusion is given in Sec. IV.

II. Simulation setups

A. Physical formulation

The simulation solves the compressible Navier–Stokes equations using the wall-resolved LES approach, which includes the conservation of mass, momentum, and total energy:

$$\frac{\partial \rho}{\partial t} + \frac{\partial \rho u_j}{\partial x_j} = 0, \tag{1}$$

$$\frac{\partial \rho u_i}{\partial t} + \frac{\partial}{\partial x_j}\left(\rho u_i u_j + p\delta_{ij}\right) = \frac{\partial \sigma_{ij}}{\partial x_j}, \tag{2}$$

$$\frac{\partial \rho e}{\partial t} + \frac{\partial}{\partial x_j}\left[\left(\rho e + p\right) u_j\right] = \frac{\partial}{\partial x_j}\left(u_i \sigma_{ij} + \kappa \frac{\partial T}{\partial x_j}\right). \tag{3}$$

The equations are written in index notation, where x_i and t are the spatial coordinate vector and time respectively. ρ is the density, u_i is the velocity vector, p is the pressure, δ_{ij} is the identity tensor, σ_{ij} is the viscous stress tensor, e is the specific total energy, κ is the total thermal conductivity, and T is the temperature. The primitive variables, ρ, u_i, and T are interpreted as the filtered quantities supported by the computational grid resolution compared to the full range of length scales of the turbulent structures. The subgrid-scale (SGS) models are absorbed into the transport properties based on the Boussinesq hypothesis [27]. The fluid is assumed to be calorically perfect with the ideal gas equation of state:

$$p = \rho R T, \tag{4}$$

where R is the specific gas constant. The total energy contains two components, $e = e_{\text{th}} + u_j u_j/2$, where the internal energy and kinetic energy are the first and second terms on the right hand side of the equation. For a calorically perfect gas, the specific internal energy can be calculated as

$$e_{\text{th}} = \frac{RT}{\gamma - 1}, \tag{5}$$

where γ is the ratio of specific heats that remains as a constant. The viscous stress tensor is calculated as

$$\sigma_{ij} = 2\mu S_{ij} + \left(\beta - \frac{2}{3}\mu\right) S_{kk}\delta_{ij}, \tag{6}$$

where μ is the total dynamic shear viscosity, β is the bulk viscosity, and S_{ij} is the rate-of-strain tensor which is calculated as

$$S_{ij} = \frac{1}{2}\left(\frac{\partial u_i}{\partial x_j} + \frac{\partial u_j}{\partial x_i}\right). \tag{7}$$

The total dynamic shear viscosity, μ, includes two components, $\mu = \check{\mu} + \mu_{\text{SGS}}$, where $\check{\mu}$ is computed using the power-law relation as a physical model:

$$\check{\mu} = \mu_{\text{ref}} \left(T/T_{\text{ref}}\right)^{0.76}, \tag{8}$$

and μ_{SGS} is calculated based on the Vreman's SGS model [28]. The bulk viscosity only considers the physical component, which is set to be directly proportional to the physical dynamic shear viscosity [29]:

$$\beta = 0.67\check{\mu}. \tag{9}$$

No SGS model is applied to the dynamic bulk viscosity in this simulation. The total thermal conductivity also contains the computable physical and SGS components, $\kappa = \check{\kappa} + \kappa_{\text{SGS}}$. The computable physical component, $\check{\kappa}$ is calculated based on a constant Prandtl number, Pr:

$$\check{\kappa} = c_p \check{\mu}/\text{Pr}, \tag{10}$$

where c_p is the specific heat at constant pressure. For a calorically perfect gas, c_p is calculated as $c_p = \gamma R/(\gamma - 1)$. The SGS component is calculated based on a constant turbulent Prandtl number, Pr_t, as follows.

$$\kappa_{\text{SGS}} = c_p \mu_{\text{SGS}}/\text{Pr}_t. \tag{11}$$

In this simulation, the physical and turbulent Prandtl numbers are set to $\text{Pr} = 0.7$ and $\text{Pr}_t = 1$ respectively.

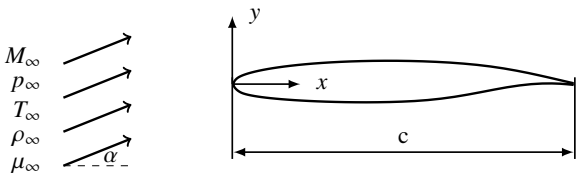

Fig. 1 Schematics of problem configuration.

Transonic flow past the OALT25 supercritical airfoil is investigated in this work. The problem configuration is shown in Fig. 1. The airfoil is placed with the chord aligned in the x-direction, and the chord length is denoted as c. The uniform free-stream conditions are specified by the Mach number M_∞ and angle of attack α. The Mach number is defined as $M_\infty = U_\infty/a_\infty$, where U_∞ and a_∞ are the flow speed and the speed of sound in the free-stream respectively. With the given thermodynamic values of T_∞ and p_∞, the speed of sound for a calorically perfect gas, can be calculated as $a_\infty = \sqrt{\gamma R T_\infty}$. The chord-based Reynolds number is defined as $\text{Re}_c = \rho_\infty U_\infty c/\mu_\infty$, where ρ_∞ and μ_∞ are the density and dynamic shear viscosity in the free-stream respectively. The free-stream is assumed to be laminar, so $\mu_{\text{SGS}} = 0$ is implied in the far-field.

B. Numerical methods

The schematic of the computational configuration is shown in Fig. 2. The computational domain is circular in the x-y plane. The domain has a radius of $R_{\text{dom}} = 70c$. The far-field flow region is regularized with the numerical sponge using the free-stream conditions. The numerical sponge layer starts from $R_{\text{spg}} = 50c$. The simulation uses a hybrid central-Riemann flux with the explicit SGS model in the regions within the radius of R_{LES}, while a pure Riemann flux, calculated using an upwind-biased shock-capturing scheme, is applied beyond the radius R_{LES}. In this work, $R_{\text{LES}} = 1.55c$ is used based on the grid resolution as well as the domain of interest.

The simulation is conducted using sixth-order compact finite difference methods [30] arranged in a high-resolution computational framework without numerical filtering [31]. Shock-capturing capability is coupled with the compact finite difference method in the convective flux discretization through a physics-based extension of the weighted compact nonlinear scheme (WCNS) approach [32–36]. The shock-capturing method is based on explicit fifth-order interpolation using the nonlinear weights of the weighted essentially non-oscillatory scheme (WENO5-Z) [37] and the Rusanov-type (local Lax–Friedrichs) Riemann flux [38] as a Riemann solver. To localize the numerical dissipation introduced by the shock-capturing scheme, the Riemann flux is hybridized with the central flux controlled by the modified Ducros sensor ϕ defined as follows:

$$\phi = \frac{-\theta|\theta| + \varepsilon^2}{\theta^2 + \boldsymbol{\omega}\cdot\boldsymbol{\omega} + \varepsilon^2}, \tag{12}$$

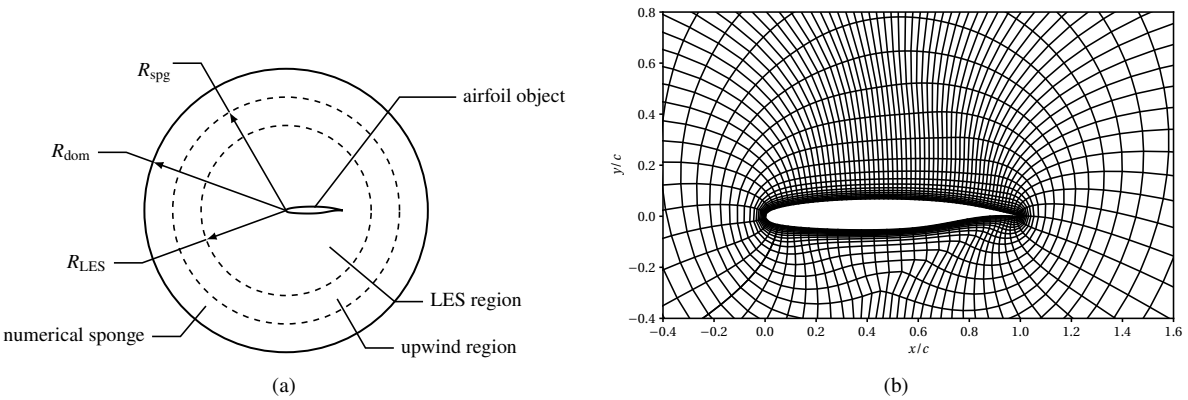

Fig. 2 Simulation configurations shown in x-y plane: (a) schematics of computational domain setup; and (b) visualization of computational mesh (down-sampled for better visualization) near the airfoil in the x-y plane. The computational domain is periodic and homogeneous in the z-dimension, with uniform computational grid spacing.

where $\theta = \nabla \cdot \boldsymbol{u}$ is the velocity dilatation, $\boldsymbol{\omega} = \nabla \times \boldsymbol{u}$ is the vorticity vector, and ε is a small constant set to $\varepsilon = 1 \times 10^{-16}$ to avoid division by zero. The simulation in this work uses binary flux blending with a specified threshold sensor value $\phi_{TH} = 0.4$. When $\phi > \phi_{TH}$, the Riemann flux is used; otherwise, only the central flux is used. The time advancement is conducted using the three-stage third-order strong-stability-preserving Runge–Kutta (SSPRK3) method [39] with an adaptive time step controlled by the global Courant–Friedrichs–Lewy (CFL) condition [40]. A CFL number of 0.95 is used for the simulation, and the time step size is mainly limited by the near-wall mesh spacing with the global CFL condition.

The simulation is deployed on an O-typed computational mesh in the x-y plane generated by smooth orthogonal hyperbolic extrusion from the airfoil geometry. To avoid spurious numerical oscillations caused by the interaction between any non-smooth geometry components and the high-order numerical schemes on a curvilinear mesh, the trailing edge starting from $x = 0.997c$ on each side of the airfoil is smoothed using a quadratic Bézier curve [41] while maintaining the original chord length. The grid size is stretched along the airfoil wall-normal direction to resolve the boundary layer flow. Since $\alpha > 0$ for the flow under investigation, the computational grid along the stream-wise direction is highly refined on the suction side to capture the shock waves and resolve the Mach waves and turbulent structures at fine scales. The computational domain is periodic in the spanwise z-direction with a span of $W = 0.25c$. The computational grid spacing is uniform in the spanwise direction. The computational mesh size is $420 \times 3072 \times 512$ in the radial, azimuthal, and span-wise directions respectively.

C. Justification of model and numerical dissipation

A brief justification of both the SGS and numerical dissipation for shock-capturing is provided by comparing the instantaneous flow fields of the numerical Schlieren imaging, the relative SGS eddy viscosity, and the modified Ducros sensor, as shown in Fig. 3. The relative SGS eddy viscosity is defined as $\mu_{SGS}/\breve{\mu}$, and the modified Ducros sensor is already stated in Eq. (12). Based on the comparison shown in Fig. 3, the SGS terms are only locally turned on in regions containing the turbulent flow features. In the near-wall region, $\mu_{SGS}/\breve{\mu} \sim O(1)$, and in the wake region farther away from the airfoil trailing edge, $\mu_{SGS}/\breve{\mu}$ is close to but still lower than 10. The use of Riemann fluxes is highly localized at shocks and strong compression waves, and the numerical dissipation from the shock-capturing scheme is essentially not in effect in the turbulence regions. Additionally, comparing the plots of μ_{SGS} and ϕ, it can be confirmed that the activation of shock-capturing scheme simultaneously suppresses the SGS model locally to avoid imposing excessive numerical dissipation, which can help capture the shock-turbulence interaction more accurately [42].

III. Results and discussions

The analysis illustrated in this section is based on the data of wall-resolved LES described in Sec. II. In this work, the free-stream Mach number of the problem is set as $M_\infty = 0.735$ and the Reynolds number is $\mathrm{Re}_c = 1 \times 10^6$. The angle

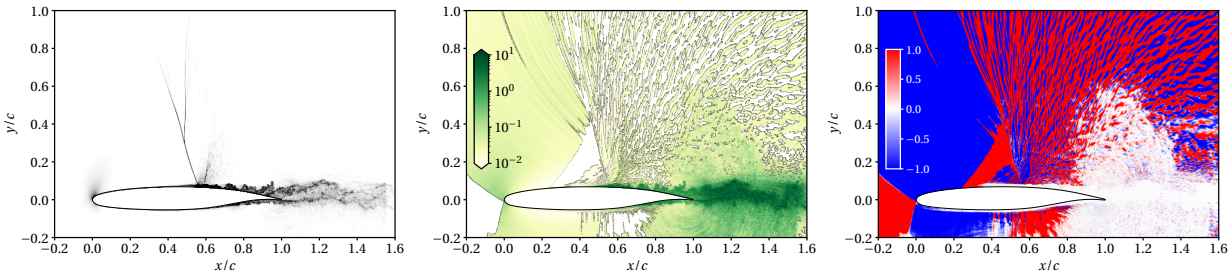

Fig. 3 Visualizations of relative model and numerical dissipation imposed in the simulation: (a) numerical Schlieren imaging; (b) ratio of SGS eddy viscosity to the physical viscosity, $\mu_{SGS}/\check{\mu}$; and (c) modified Ducros sensor, ϕ, shown in Eq. (12), where shock-capturing scheme is used when $\phi > 0.4$.

of attack is chosen to be $\alpha = 4^\circ$ for shock buffet to occur. The simulation time is normalized by the convective time unit (CTU), which is defined as $1 \times \text{CTU} = c/U_\infty$. After the initial transient stage, the simulation data are collected at a fixed time interval, about 0.02174 CTUs. Data, including 8192 snapshots, are used for post-simulation analysis, which is over a span of approximately 178 CTUs. In the following context, the visualization-based observation of shock buffet and the related flow structures is described in Sec. III.A. Detailed analysis of signals at selected probe locations is illustrated in Sec. III.B. Finally, the low-rank model analysis based on the spectral proper orthogonal decomposition (SPOD) is discussed in Sec. III.C.

A. Visualizations of shock buffet and related flow structures

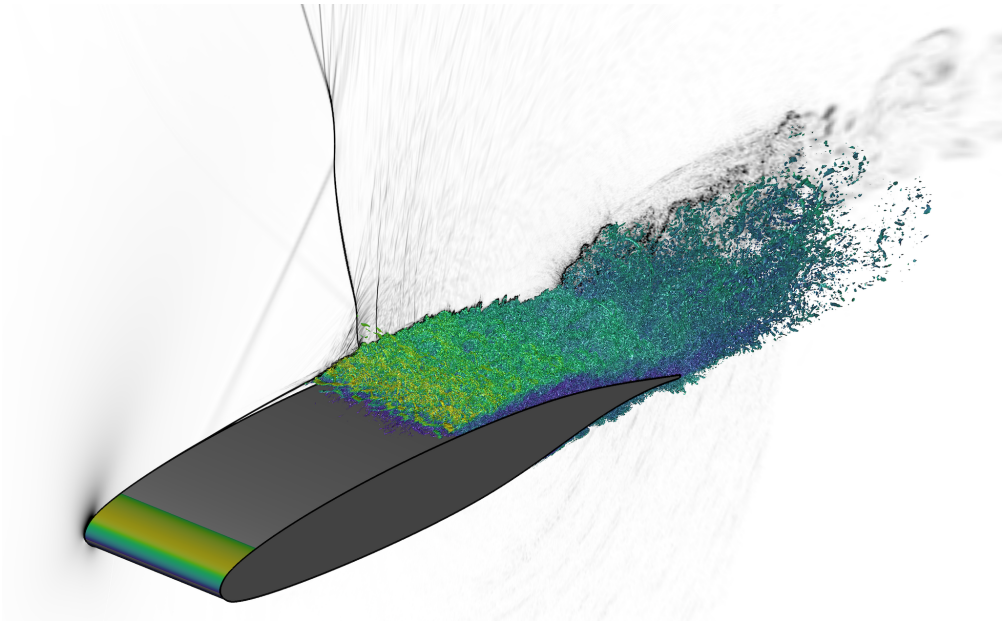

Fig. 4 Visualization of 3D instantaneous flow fields at around 137th CTU around the gray airfoil geometry, where the cross-sectional view shows numerical Schlieren imaging and the iso-surfaces show Q-criterion at the value of around 2644.4. The iso-surface is colored by the value of local Mach number.

An instantaneous three-dimensional (3D) flow visualization is shown in Fig. 4. The visualization contains cross-sectional numerical Schlieren imaging, indicated by $|\nabla\rho|\,(c/\rho_\infty)$, and iso-surfaces of the normalized Q-criterion at a

value of around 2644.4. The definition of the normalized Q-criterion used in this work is

$$Q = \frac{1}{2}\left(\theta^2 + \frac{1}{2}\omega_j\omega_j - S_{ij}S_{ij}\right)\left(\frac{c}{U_\infty}\right)^2.$$

The iso-surfaces are colored by the local Mach number. The visualization indicates that the subsonic free-stream flow accelerates to supersonic conditions through an expansion near the leading edge. The flow on the suction side is initially laminar from the leading edge. Then, the boundary layer separates and transitions to turbulence. A strong compression wave (weak oblique shock) / the front-branch of a λ-shock forms in front of the laminar separation points and interacts with the laminar boundary layer. The main shock forms slightly after the boundary layer transitions to turbulence. A terminating shock behind the main shock is observed in the visualization at this time instant. This is similar to what is shown in some of the simulation cases of the same airfoil at different Reynolds numbers [21]. The transitional turbulent boundary layer generates strong acoustic waves which propagate into the slightly far-field regions. Turbulent vortex shedding associated with the unsteadiness of the transitional separated boundary layer also occurs. The turbulent structures, visualized by the Q-criterion, suggest sufficient decorrelation in the span-wise periodic and homogeneous computational domain of a quarter of a chord length.

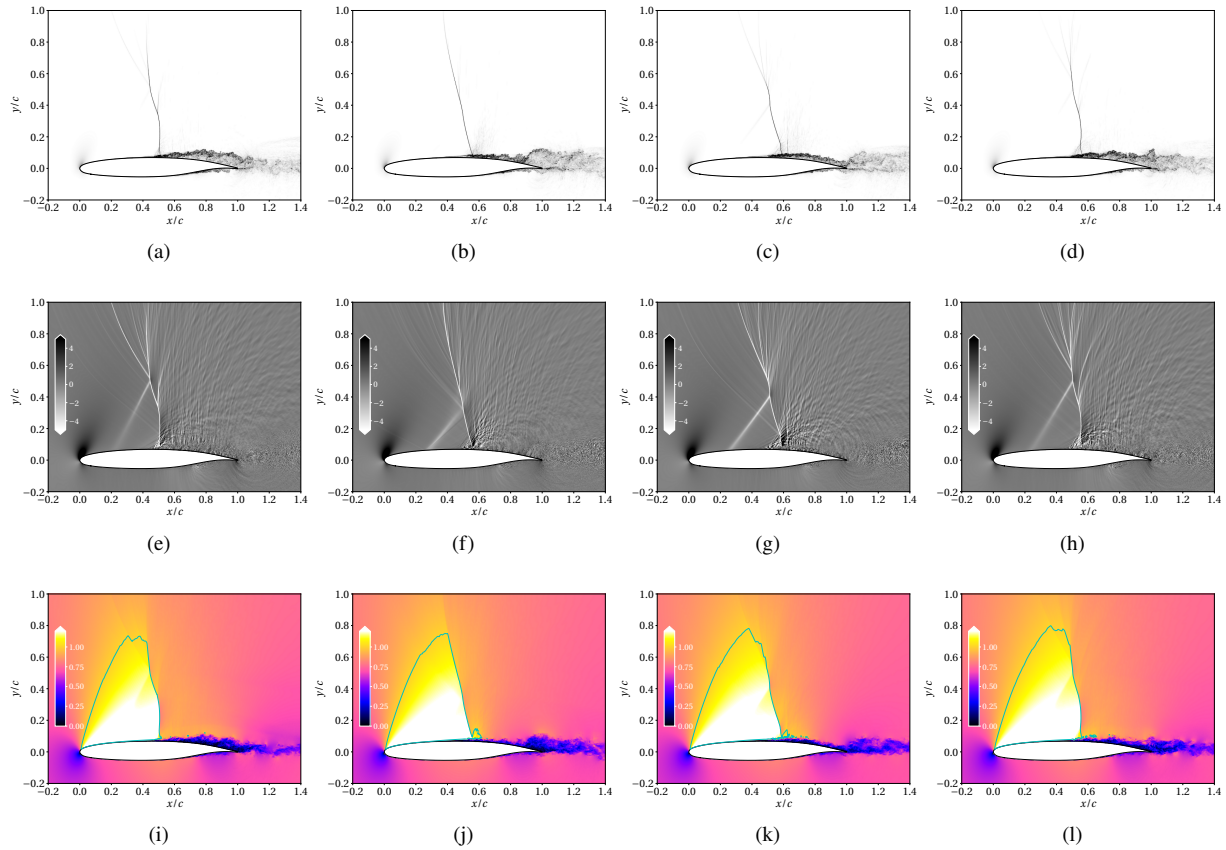

Fig. 5 Visualization of 2D instantaneous flow fields: (a)–(d) numerical Schlieren imaging; (e)–(h) velocity dilatation; (i)–(l) local Mach number with sonic lines marked. The visualizations are given at 131.8th CTU for (a), (e), and (i), 134.2th CTU for (b), (f), and (j), 136.6th CTU for (c), (g), and (k), and 139.0th CTU for (d), (h), and (l).

A set of two-dimensional (2D) visualizations is shown in Fig. 5 at four successive time instants with an approximately fixed time interval between them. Combined with the 3D visualization, Fig. 5 shows that the up-travelling waves originating from the turbulent boundary layer become steeper along their propagation direction into the slightly far-field regions and form large-scale wave fronts. Some steepened waves merge and form short-lasting shocks. Across the main shock, the flow changes from supersonic to subsonic. Near the back of the main shock foot region, an expansion region periodically forms where the flow re-accelerates to supersonic state. The re-accelerated flow eventually switches

back to subsonic again through a periodically formed terminating shock which is caused by the steepening of the up-traveling strong acoustic waves in the re-accelerated supersonic flow. Based on the observation, after-shock expansion and terminating shock mostly form behind a retreating shock that moves towards the trailing-edge direction. While the main shock moves downstream, the expansion wave is strengthened. The terminating shock forms at the end of expansion region and is being pushed farther downstream. When the main shock moves upstream, the expansion wave becomes weaker. The terminating shock also moves forward and eventually merges into the advancing main shock. The up-traveling acoustic waves originating from the turbulent wake also steepen while they are propagating upstream and interact with the flow near the main shock region.

B. Analysis of aerodynamic coefficients and locally probed signals

The pressure coefficient, $C_p = 2(p - p_\infty)/(\rho_\infty U_\infty^2)$, and skin-friction coefficient, $C_f = 2\tau_w/(\rho_\infty U_\infty^2)$, are measured at the airfoil surface, where τ_w is the local wall shear stress. The results are averaged in both span-wise direction and time. The distribution of C_p and C_f and their temporal fluctuation magnitude, indicated by the symmetric intervals of their standard deviations of the span-wise averaged values, are shown in Fig. 6. Combined with the visualizations shown in Sec. III.A, it is seen that in the region where the foot of λ-compression wave / shock in front of the laminar separation point ($0.2 < x/c < 0.3$) occurs, large fluctuations in C_p and C_f are observed compared to the neighboring regions. The laminar separation point mostly varies in the region of $0.30c - 0.42c$. After the flow transitions to turbulence, significant fluctuations in both C_p and C_f are observed due to the turbulent vortex shedding.

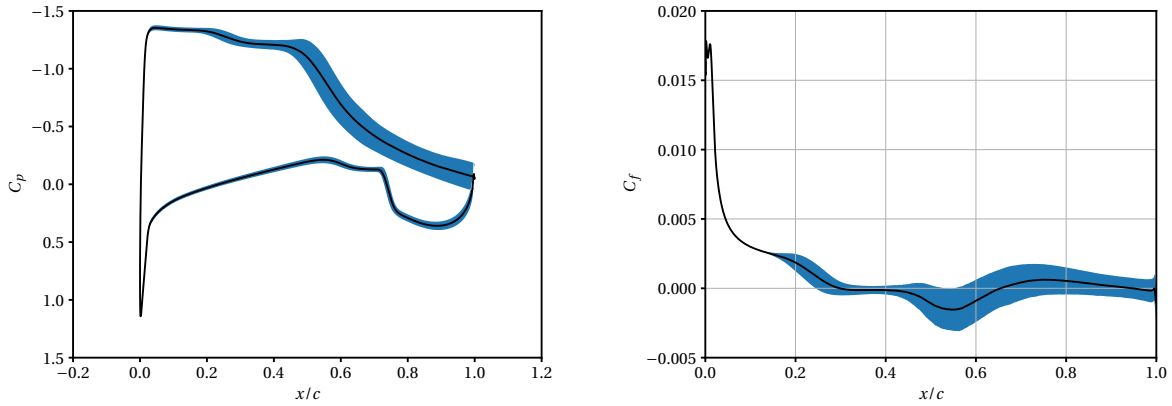

Fig. 6 Distributions of mean C_p and C_f , their fluctuations indicated by the symmetric intervals of their temporal standard deviations (marked by the blue shading). The plot of C_f only shows the distribution on the suction side.

To further investigate the time history, the x-t diagram of C_f on the suction side and the power spectral density (PSD) are provided in Fig. 7. The PSD is generated using the discrete Fourier transform in the time dimension. Welch's method [43] is applied to achieve a better convergence of statistics, and each windowed data segment contains 3072 snapshots and 87.5% overlap between each sequential segment. The Hann window is applied to each segment to prevent spectral leakage. In addition, the PSDs are normalized using the U_∞/c and the squared reference value for each quantity (if the quantity is not normalized). For instance, p_∞^2 is the squared reference value used for the pressure. Comparing the x-t diagram of C_f shown in Fig. 7 with the flow visualizations in Fig. 5, the strong negative C_f near $x/c = 0.5$ is caused by the flow separation and transition to turbulence in the separate flow. The oscillation, or periodic growing and detaching, of the separation bubbles is strongly correlated with the vortex shedding. The propagation of shedding vortices is characterized by the interleaved trajectories of the positive and negative contours of C_f in the x-t diagram in the region where $x/c > 0.6$. The PSD of C_f in Fig. 7 indicates that such vortex shedding is at the non-dimensional frequency $\mathrm{St} \approx 0.55$, where for a given dimensional frequency f, the definition of the non-dimensional frequency, also known as the Strouhal number, is defined as $\mathrm{St} = fc/U_\infty$. Along the x-dimension in the PSD contour, higher fluctuation energy locates in the foot of λ-compression wave / shock region ($0.2 < x/c < 0.3$) and turbulent flow region ($x/c > 0.6$). In contrast, relatively less fluctuation energy is measured by C_f near the laminar separation point ($x/c \approx 0.3$). Along

the St-dimension, a peak at lower frequency, St ≈ 0.1 is detected beside the shedding frequency at St ≈ 0.55, which is also observed in the x-t diagram in Fig. 7a. The corresponding location of the peak at the frequency of St ≈ 0.1 is near $0.5 < x/c < 0.7$ where the main shock, expansion wave, and terminating shock appear.

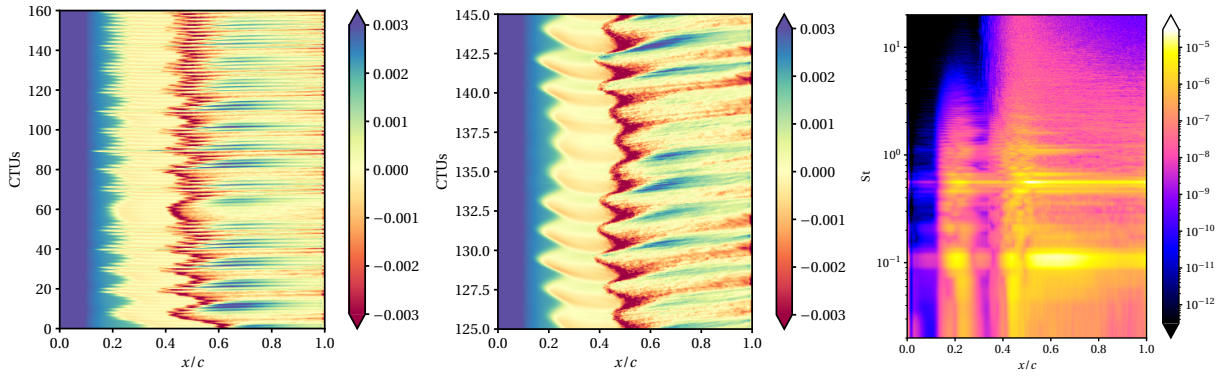

Fig. 7 Temporal variation of the span-wise averaged C_f on the suction side: (a) x-t diagram within a range of 160CTUs; (b) zoomed-in x-t diagram within a range of 20CTUs; (c) spatial distribution of PSD.

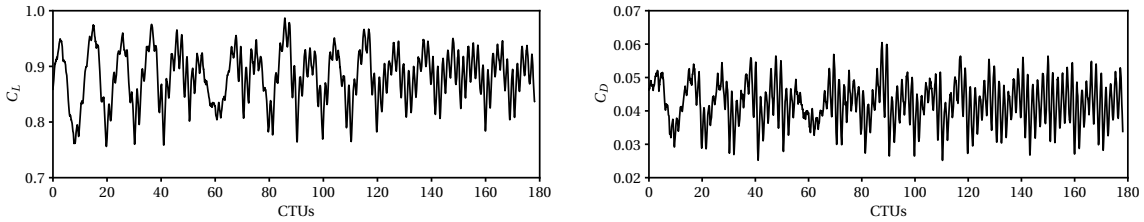

Fig. 8 Time histories of (a) lift coefficient, C_L, and (b) drag coefficient, C_D.

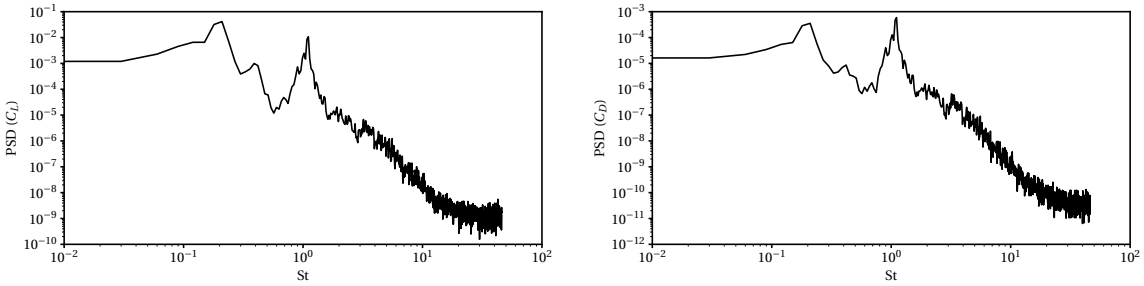

Fig. 9 PSD plots of (a) lift coefficient, C_L, and (b) drag coefficient, C_D.

The time series of lift coefficient, C_L, and drag coefficient, C_D are shown in Fig. 8, and their PSDs are shown in Fig. 9. The lift and drag coefficients are calculated by integrating the pressure and shear stress over the whole airfoil.

$$C_{L,D} = \frac{1}{A_{\text{airfoil}}} \oint_{\text{airfoil}} \left(C_f \hat{\boldsymbol{t}} - C_p \hat{\boldsymbol{n}}\right) \cdot \hat{\boldsymbol{e}}_{L,D} dA$$

where A_{airfoil} is the total area of the airfoil surface, $\hat{\boldsymbol{t}}$ is the unit tangential vector of the airfoil in the x-y plane, $\hat{\boldsymbol{n}}$ is the unit outgoing normal vector of the airfoil geometry, and $\hat{\boldsymbol{e}}_{L,D}$ is the unit reference vector. For the calculation of C_L, $\hat{\boldsymbol{e}}_L = -\hat{\boldsymbol{e}}_x \sin\alpha + \hat{\boldsymbol{e}}_y \cos\alpha$, and for the calculation of C_D, $\hat{\boldsymbol{e}}_D = \hat{\boldsymbol{e}}_x \cos\alpha + \hat{\boldsymbol{e}}_y \sin\alpha$, where $\hat{\boldsymbol{e}}_x$ and $\hat{\boldsymbol{e}}_y$ are the unit vectors in the x and y directions respectively. The oscillations of C_L and C_D, as the integrated aerodynamic coefficients, also contains the two dominant frequencies, same as the values measured in the C_f profile on the suction side, where the oscillation at St ≈ 0.55 is identified as caused by the turbulent vortex shedding.

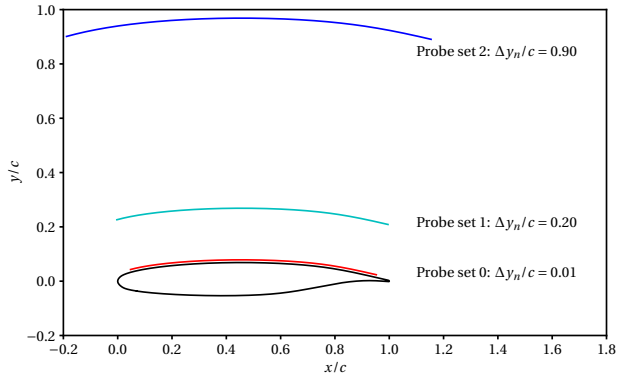

Fig. 10 Schematic of probing locations relative to the airfoil.

In order to further investigate the Strouhal number at St ≈ 0.1, three line sets of numerical probes are placed at fixed locations to sample the local signals in time. The locations are determined by normal extrusion of the airfoil surface on the suction side from $x/c = 0.05$ to $x/c = 0.95$. The normal extrusion displacements, Δy_n, are set to $0.01c$, $0.2c$, $0.9c$. At each reference surface in the x-y plane, 512 numerical probes are created. The labeling nomenclature of the numerical probes and their locations are shown in Fig. 10. The probe set 0 is used to diagnose the near-wall region, the probe set 1 is used to measure the main shock buffet, and the probe set 2 is used to sense the flow outside the sonic line.

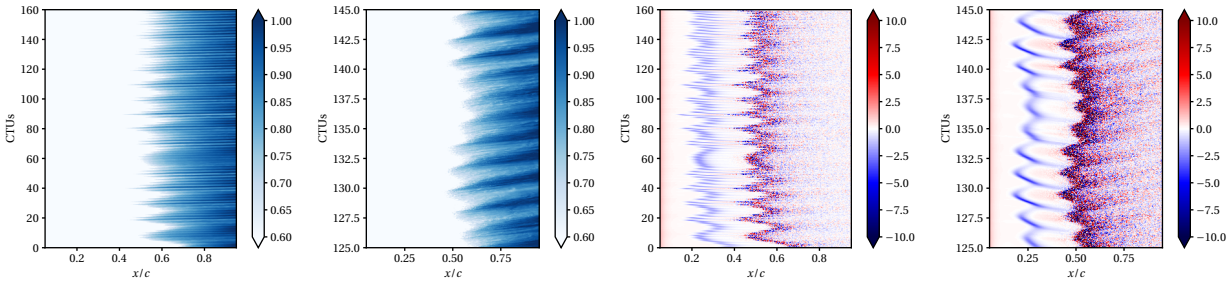

Fig. 11 x-t diagrams of data collected by the probe set 0: (a), (b) pressure (normalized by p_∞); and (c), (d) velocity dilatation (normalized by U_∞/c). (b) and (d) zoom in a shorter range of time compared to (a) and (c) respectively.

The pressure and velocity dilatation collected by the line probe sets 0, 1, and 2 are shown in Fig. 11, Fig. 12, and Fig. 13 respectively as x-t diagrams. Both the short-term (range of 20 CTUs) and long-term (range of 160 CTUs) are plotted. At the probe set 0 location, both transition and vortex shedding are captured by the pressure and dilatation signals. Moreover, the dilatation x-t diagram also captures the motion of the λ-compression wave / shock in front of the laminar separation point. Its unsteadiness highly correlates with vortex shedding. Additionally, the lower frequency can be observed in the long-term x-t diagram. It can be also seen that strong fluctuating dilatational motion occurs in the region where flow transitions to turbulence which creates strong acoustic radiation. The location of the probe set 2 is set in the free-stream region across the main shock location. Both pressure and velocity dilatation signals clearly capture the main shock buffet as shown in Fig. 13. It can be seen that the main shock buffet is primarily at the low-frequency, but its buffet trajectory is also affected by the vortex shedding frequency. Specifically from the dilatation x-t diagram in

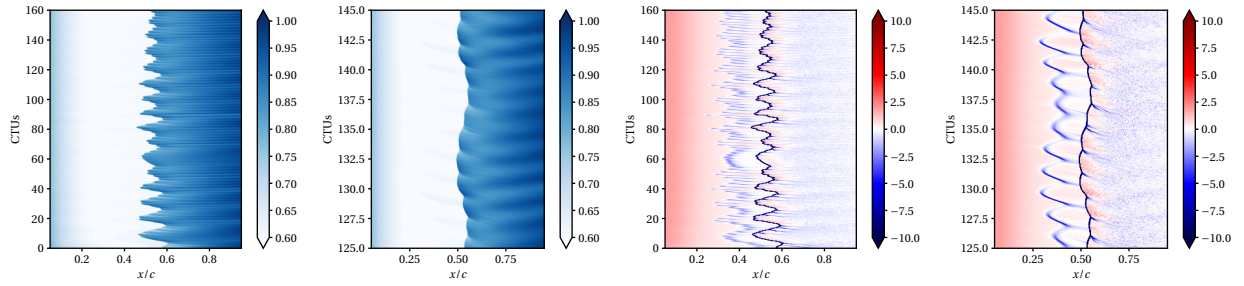

Fig. 12 x-t diagrams of data collected by the probe set 1: (a), (b) pressure (normalized by p_∞); and (c), (d) velocity dilatation (normalized by U_∞/c). (b) and (d) zoom in a shorter range of time compared to (a) and (c) respectively.

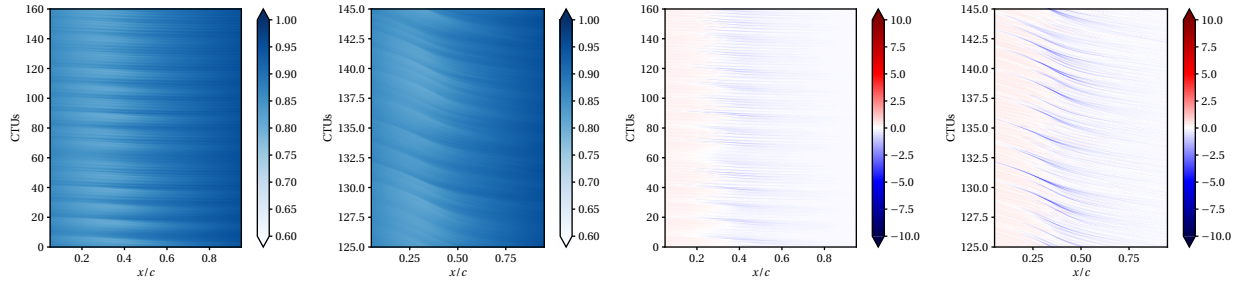

Fig. 13 x-t diagrams of data collected by the probe set 2: (a), (b) pressure (normalized by p_∞); and (c), (d) velocity dilatation (normalized by U_∞/c). (b) and (d) zoom in a shorter range of time compared to (a) and (c) respectively.

Fig. 12 the formation of strong compression waves behind the main shock which partially extended from the terminating shock in the lower region can be observed, and these waves eventually merge into the main shock. In between, the x-t diagram also captures the periodic expansion waves after the main shock. The signals outside the sonic line collected by the probe set 2 shown in Fig. 13 are dominated by the upstream-traveling waves, and the signal variations contain both higher and lower frequencies as observed from the signals sensed by other sets of probes.

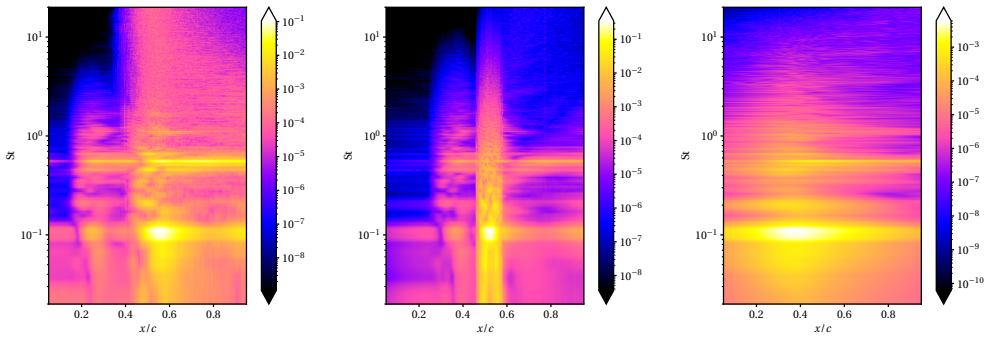

Fig. 14 Normalized PSD contours of pressure signals at the locations of (a) probe set 0, (b) probe set 1, and (c) probe set 2.

The PSD contours of the pressure signals sampled by all three line probe sets are shown in Fig. 14. By comparison, it can be seen that the signal at all three locations have the same two dominant frequencies at St ≈ 0.1 and St ≈ 0.55 respectively. Additionally, in Fig. 14b the high spectral energy is mostly peaked in the region where $0.5 < x/c < 0.6$ and St ≈ 0.1. This feature confirms that the low-frequency peak at St ≈ 0.1 is the shock buffet Strouhal number. With this, revisiting the PSD of C_f shown in Fig. 7, besides the regular turbulent vortex shedding at St ≈ 0.55, the motion of the compression wave / λ-shock, laminar separation points, transition to turbulence, and variation vortex shedding at a longer time range are all correlated with the shock buffet Strouhal number at St ≈ 0.1. It can be also seen that both vortex shedding and shock buffet strongly affect the variations of the integrated aerodynamic coefficients, C_L and C_D.

C. Low-rank modal analysis

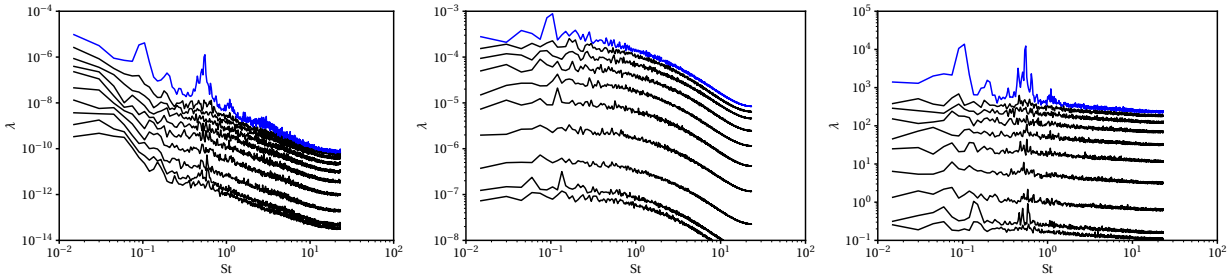

(a) (b) (c)

Fig. 15 Spectra of the top 10 eigenvalues at each Strouhal number obtained by (a) pressure norm, p, (b) density weighted dilatation norm, $\rho\theta$, and (c) enstrophy norm, $\rho\omega_j\omega_j/2$.

To further investigate the correlation between the shock buffet and other flow structures, a low-rank modal analysis is conducted using SPOD [44, 45]. SPOD is a special form of the more popular "standard" proper orthogonal decomposition (POD) method which was introduced as a data-driven approach to the study of fluid mechanics by Lumley [46]. In this approach, POD modes are extracted using the two-point spatial correlation tensor based on the chosen definition of energy norm or inner product. These POD modes are the most optimal modes in which a subset of the modes can reconstruct a large portion of the energy defined by the inner product. The spectral POD, or SPOD, is different from the "standard" POD as the former has a space-time decomposition under the assumption that the flow data is statistically stationary while the latter only considers correlation in space and not the sequential ordering of data in time. As a result, SPOD can extract modes that are coherent in both space and time while the "standard" POD only gives spatially coherent modes [44]. While SPOD has been re-introduced recently [44, 45], much of the original literature relating to it stems from the early works by Lumley [46, 47]. SPOD has been used for the analysis of different turbulent flows, such as jet flows [48, 49], wakes behind a disk [50], channel flows [51], flows past aerodynamic devices [14, 21, 52, 53], etc.

In this work, SPOD analysis is conducted with three different scalar energy norms including pressure, p, density weighted dilatation, $\rho\theta$, and enstrophy, $\rho\omega_j\omega_j/2$. The settings of the SPOD solver are similar to those used for PSD calculations. The bin size is set to 3072 with 87.5% overlap between each neighboring bins. With 8192 total data snapshots used in this study, a total of 14 bins can be obtained. The top 10 eigenvalues, λ, at each frequency in the descending order of the energy are plotted in Fig. 15. All three scalar energy norms can detect the shock buffet mode at St ≈ 0.1 because of the presence of the peaks at the corresponding Strouhal number in the spectra. The pressure and enstrophy norms are able to clearly capture the vortex shedding mode at a higher Strouhal number of St ≈ 0.55. As expected, the dilatation norm is not sensitive to the vortex shedding mode since vortex shedding does not cause dilatation as strong as shocks. At each peak of the first eigenvalue profile, clearly low-rank behavior is obtained since the first mode is much more energetic than the other modes. Three representative energetic SPOD eigenmodes, at $St_1 \approx 0.105$, $St_2 \approx 0.554$, and $St_3 \approx 1.093$ are selected for further investigation of their eigenvector behaviors. The SPOD mode at St_3 has been reported as the mode corresponding to the boundary layer separation and free-transition due to the Kevin–Helmholtz instability in the prior studies [20, 21, 25]. The selected modes are marked in Fig. 16.

The eigenvectors calculated using all three scalar energy norms at the shock buffet Strouhal number ($St_1 \approx 0.105$) are shown in Fig. 17. The eigenmodes are visualized at four different phase angles, φ, within the range of $\varphi \in [0, \pi)$,

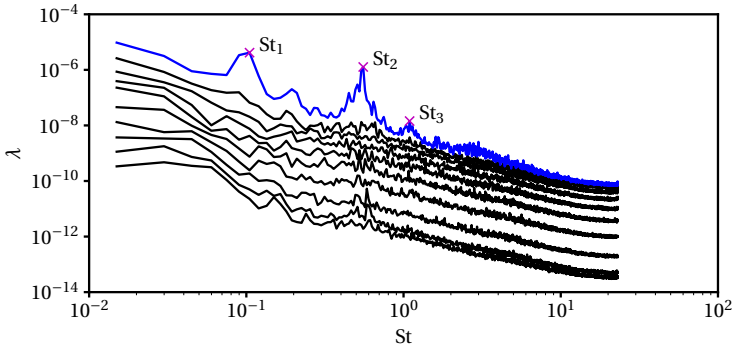

Fig. 16 Selected SPOD eigenmodes at $St_1 \approx 0.105$, $St_2 \approx 0.554$, and $St_3 \approx 1.093$, plotted with the SPOD eigenvalue spectra of pressure.

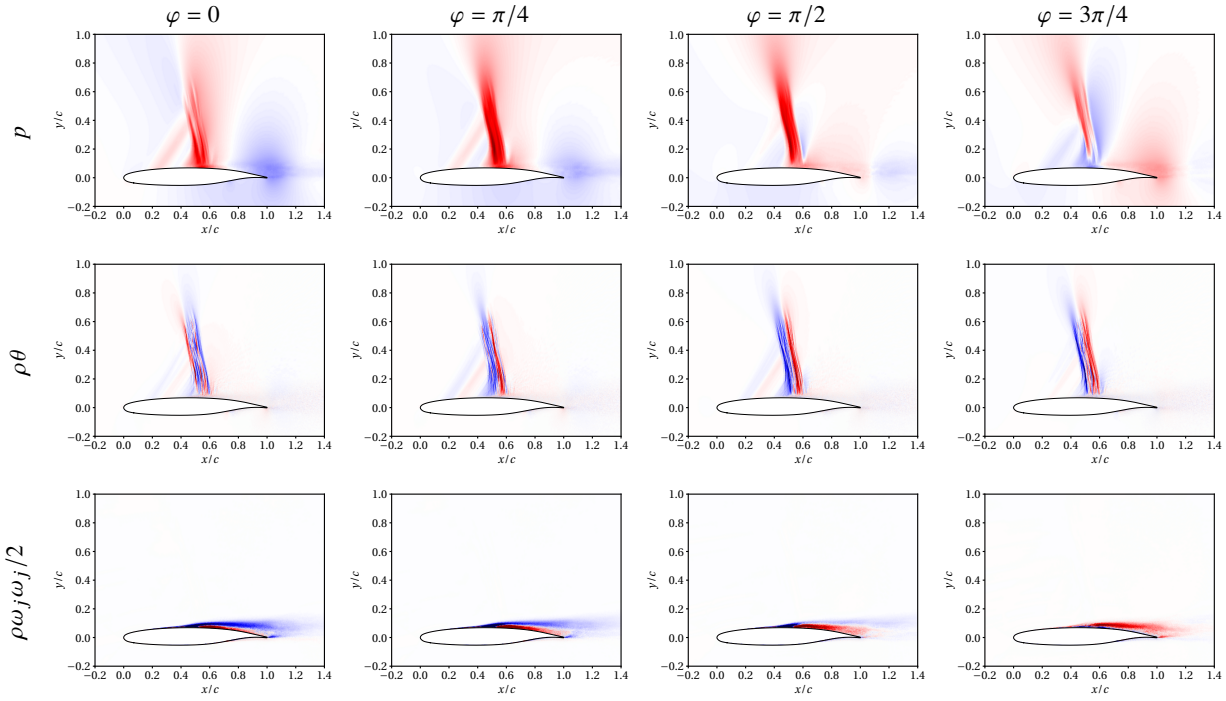

Fig. 17 The first SPOD mode at the shock buffet Strouhal number ($St_1 \approx 0.105$) obtained with the pressure norm (first row), density-weighted dilatation norm (second row), and enstrophy norm (third row). The eigenmodes are visualized at four phase angles, φ, within the range of $\varphi \in [0, \pi)$.

with the phase angle defined as $\varphi = 2\pi \mathrm{St}\tau$ where St is the Strouhal number and $\tau = tU_\infty/c$ is the non-dimensional time. The eigenvector calculated by the pressure norm captures the low-frequency variation in the turbulent vortex shedding, which is consistent with that calculated by the enstrophy norm. Near the trailing edge, this mode propagates downstream. However, closely behind the main shock foot, the information travels upwards outside the sonic line and propagates upstream. This behavior is captured by the SPOD modes calculated by both pressure and dilatation norms. The observation is consistent with what is reported in the study of turbulent shock buffet using resolvent analysis [14]. Combined with the flow visualizations, this mode is highly correlated with the periodic formations of expansion waves and terminating shocks. Furthermore, the pressure mode also reveals the upstream traveling waves originating from the trailing edge on the pressure side of the airfoil. The eigenmode calculated from the enstrophy norm also reveals the low-frequency movement of the laminar-to-turbulent transition point. This behavior shows synchronized response in the separated region causing the low-frequency breathing in the separated turbulent region behind the main shock at a

chord-length scale.

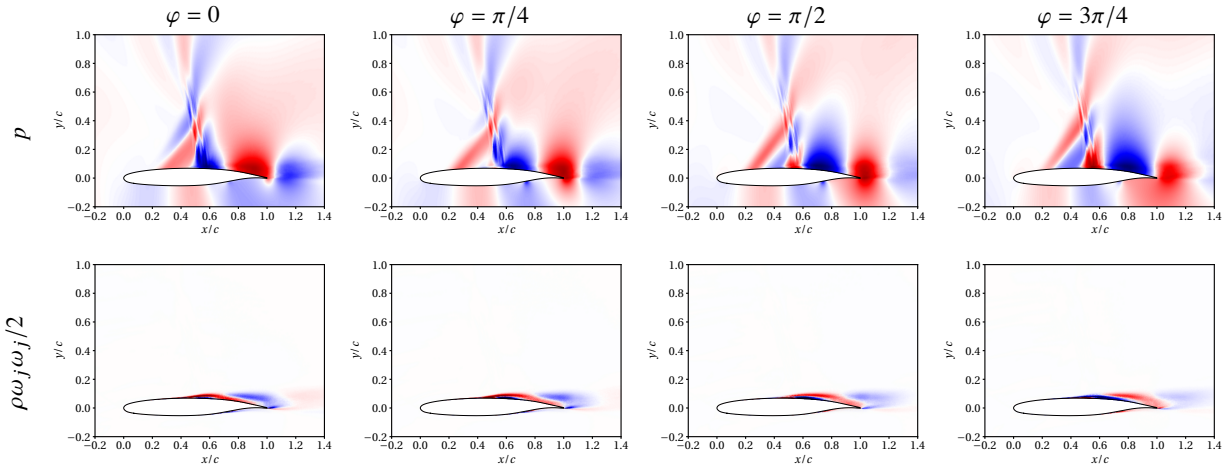

Fig. 18 The first SPOD mode at the turbulent vortex shedding Strouhal number ($St_2 \approx 0.554$) obtained with the pressure norm (first row) and enstrophy norm (second row). The eigenmodes are visualized at four phase angles within the range of $\varphi \in [0, \pi)$.

The eigenmodes calculated with the pressure and enstrophy norms at the turbulent vortex shedding Strouhal number ($St_2 \approx 0.554$) are shown in Fig. 18. Near the trailing-edge, the pressure SPOD mode indicates the non-radiating pseudo-sound behavior associated with the shedding vortex. The enstrophy SPOD mode indicates the evolution of the separation bubble which contributes to the successive formation of the shedding vortices. Similar to the SPOD modes at the buffet Strouhal number, St_1, upstream-travelling waves above the sonic line are observed over the shock, which creates possibility for a feedback control loop. These waves are from both the regions behind the main shock foot as well as the vortex street. It is also observed from the pressure SPOD mode that the information originating in front of the main shock foot propagates through the shock from the near-wall low speed region. The wave passing through the shock foot contributes to both vortex shedding and upward propagation waves behind the shock to form the feedback control loop. Additionally, a portion of the wave originating in front of the shock foot propagate upstream within the boundary layer and enters the external flow. These waves continuously merge into the λ-compression wave / shock. Furthermore, upstream traveling waves on the pressure side are also observed.

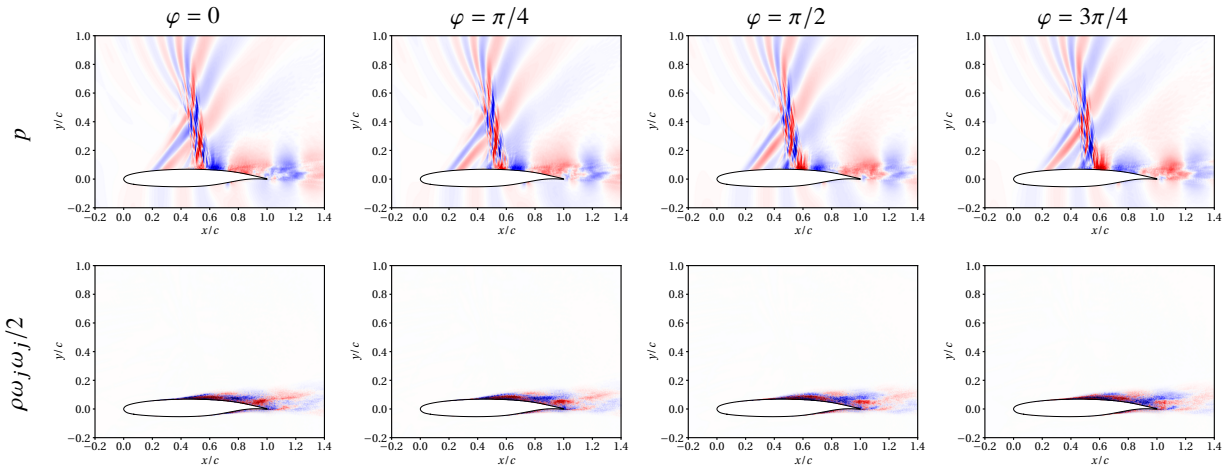

Fig. 19 The first SPOD mode at the laminar separation Strouhal number ($St \approx 1.093$) obtained with different energy norms. The eigenmodes are visualized within the range of phase angle $\varphi \in [0, \pi)$.

The pressure and enstrophy mode shapes at the boundary layer separation / free-transition Strouhal number

($St_3 \approx 1.093$) are shown in Fig. 19. Unlike the simulation of the same airfoil at higher Reynolds number reported in the prior study [20], neither pressure or enstrophy modes at this Strouhal number carries dominant energy as strong as those of the modes at the shock buffet Strouhal number and vortex shedding Strouhal number. Nevertheless, the pressure mode shape shows a wide range of spatial correlation, and the wave pattern is similar to that at the vortex shedding Strouhal number ($St_2 \approx 0.554$). Compared to the vortex shedding mode, the separation mode includes finer scale features. It is also noted that this laminar separation / free-transition Strouhal number is overlapped in the range of potential harmonic mode of the vortex shedding Strouhal number.

IV. Conclusions

A high-resolution wall-resolved LES of a transonic flow over the OALT25 laminar supercritical airfoil was performed at $M_\infty = 0.735$, $\mathrm{Re}_c = 1 \times 10^6$, and $\alpha = 4°$. The simulation was conducted using high-order compact finite difference methods with hybrid central-Riemann fluxes. The use of the shock-capturing scheme is controlled by a physics-based shock sensor, and the numerical dissipation from the shock-capturing is not imposed in the turbulence region. Data including 8192 snapshots over a span of approximately 178 CTUs were used in the analysis. The instantaneous flow and wave structures were visualized and discussed. The flow conditions were locally sensed on the airfoil surface and at three reference lines created via orthogonal extrusion of the airfoil wall boundary on the suction side during the simulations. Clear shock buffet phenomenon was observed in both flow visualization and the x-t diagram of velocity dilatation sensed in the free-stream above the suction side of the airfoil. Two dominant Strouhal numbers were detected from the variations of the integrated aerodynamic coefficients, C_L and C_D. The lower Strouhal number is at $\mathrm{St} \approx 0.1$, which is identified to be due to the shock buffet. The higher Strouhal number is at $\mathrm{St} \approx 0.1$, which is caused by the turbulent vortex shedding. SPOD analysis was conducted using the scalar norms of pressure, density-weighted dilatation, and enstrophy respectively. The shock buffet frequency are captured by all three norms. The eigenvalue spectra calculated using the pressure norm and enstrophy norm also capture the vortex shedding frequency. The SPOD eigenmodes at three selected Strouhal numbers, corresponding to the shock buffet ($St_1 \approx 0.105$), vortex shedding ($St_2 \approx 0.554$), and laminar separation / free-transition which were identified in the related study [20, 21, 25], ($St_3 \approx 1.093$), were visualized. The result implies that the flow fluctuation near the main shock foot associated with the evolution of separation bubble movement of the point of laminar separation and transition to turbulence, periodic formation of the expansion waves and terminating shocks, etc., plays an important role in affecting the shock buffet behavior. Upstream traveling waves above the supersonic region on the suction side were observed from both SPOD analysis and probe signals, which form a possible feedback loop mechanism.

Acknowledgements

This work is supported by the National Science Foundation (NSF), grant number NSF-OAC-2103509. The simulation was supported by an INCITE allocation and run on the *Summit* supercomputer from the Oak Ridge Leadership Computing Facility at the Oak Ridge National Laboratory, which is supported by the Office of Science of the U.S. Department of Energy under Contract No. DE-AC05-00OR22725. The OALT25 airfoil geometry is provided by ONERA. The authors are grateful to Dr. Brion Vincent for the help in accessing the original OALT25 airfoil profile.

References

[1] Lee, B., "Self-sustained shock oscillations on airfoils at transonic speeds," *Progress in Aerospace Sciences*, Vol. 37, No. 2, 2001, pp. 147–196.

[2] Giannelis, N. F., Vio, G. A., and Levinski, O., "A review of recent developments in the understanding of transonic shock buffet," *Progress in Aerospace Sciences*, Vol. 92, 2017, pp. 39–84.

[3] Jacquin, L., Molton, P., Deck, S., Maury, B., and Soulevant, D., "Experimental study of shock oscillation over a transonic supercritical profile," *AIAA journal*, Vol. 47, No. 9, 2009, pp. 1985–1994.

[4] McDevitt, J. B., and Okuno, A. F., "Static and dynamic pressure measurements on a NACA 0012 airfoil in the Ames high Reynolds number facility," Tech. rep., 1985.

[5] Benoit, B., and Legrain, I., "Buffeting prediction for transport aircraft applications based on unsteady pressure measurements," *5th Applied Aerodynamics Conference*, 1987, p. 2356.

[6] Brunet, V., "Computational study of buffet phenomenon with unsteady RANS equations," *21st AIAA Applied Aerodynamics Conference*, 2003, p. 3679.

[7] Goncalves, E., and Houdeville, R., "Turbulence model and numerical scheme assessment for buffet computations," *International Journal for Numerical Methods in Fluids*, Vol. 46, No. 11, 2004, pp. 1127–1152.

[8] Iovnovich, M., and Raveh, D. E., "Reynolds-averaged Navier-Stokes study of the shock-buffet instability mechanism," *AIAA journal*, Vol. 50, No. 4, 2012, pp. 880–890.

[9] Deck, S., "Numerical simulation of transonic buffet over a supercritical airfoil," *AIAA journal*, Vol. 43, No. 7, 2005, pp. 1556–1566.

[10] Grossi, F., Braza, M., and Hoarau, Y., "Prediction of transonic buffet by delayed detached-eddy simulation," *AIAA Journal*, Vol. 52, No. 10, 2014, pp. 2300–2312.

[11] Zangeneh, R., "Parametric study of separation and reattachment in transonic airfoil flows," *AIAA Journal*, Vol. 59, No. 11, 2021, pp. 4465–4474.

[12] Fukushima, Y., and Kawai, S., "Wall-modeled large-eddy simulation of transonic airfoil buffet at high Reynolds number," *AIAA journal*, Vol. 56, No. 6, 2018, pp. 2372–2388.

[13] Balakumar, P., Iyer, P. S., and Malik, M. R., "Turbulence Simulations of Transonic Flows over an NACA-0012 Airfoil," *AIAA SCITECH 2023 Forum*, 2023, p. 0254.

[14] Iwatani, Y., Asada, H., Yeh, C.-A., Taira, K., and Kawai, S., "Identifying the Self-Sustaining Mechanisms of Transonic Airfoil Buffet with Resolvent Analysis," *AIAA Journal*, 2023, pp. 1–12.

[15] Gur, O., Schetz, J. A., and Mason, W. H., "Aerodynamic considerations in the design of truss-braced-wing aircraft," *Journal of Aircraft*, Vol. 48, No. 3, 2011, pp. 919–939.

[16] Zauner, M., and Sandham, N. D., "Modal analysis of a laminar-flow airfoil under buffet conditions at Re= 500,000," *Flow, Turbulence and Combustion*, Vol. 104, No. 2-3, 2020, pp. 509–532.

[17] Brion, V., Dandois, J., Abart, J.-C., and Paillart, P., "Experimental analysis of the shock dynamics on a transonic laminar airfoil," *Progress in Flight Physics–Volume 9*, Vol. 9, 2017, pp. 365–386.

[18] Placek, R., and Miller, M., "Wind Tunnel Tests of Laminar–Turbulent Transition Influence on Basic Aerodynamic Characteristics of Laminar Airfoil in Transonic Flow Regime," *Inst. of Aviation TR D-5.2*, Vol. 2, 2016.

[19] Placek, R., and Ruchała, P., "The flow separation development analysis in subsonic and transonic flow regime of the laminar airfoil," *Transportation Research Procedia*, Vol. 29, 2018, pp. 323–329.

[20] Dandois, J., Mary, I., and Brion, V., "Large-eddy simulation of laminar transonic buffet," *Journal of Fluid Mechanics*, Vol. 850, 2018, pp. 156–178.

[21] Zauner, M., Moise, P., and Sandham, N. D., "On the co-existence of transonic buffet and separation-bubble modes for the OALT25 laminar-flow wing section," *Flow, Turbulence and Combustion*, Vol. 110, No. 4, 2023, pp. 1023–1057.

[22] Grossi, F., "Physics and modeling of unsteady shock wave/boundary layer interactions over transonic airfoils by numerical simulation," Ph.D. thesis, 2014.

[23] Szubert, D., Asproulias, I., Grossi, F., Duvigneau, R., Hoarau, Y., and Braza, M., "Numerical study of the turbulent transonic interaction and transition location effect involving optimisation around a supercritical aerofoil," *European Journal of Mechanics-B/Fluids*, Vol. 55, 2016, pp. 380–393.

[24] Sznajder, J., and Kwiatkowski, T., "Analysis of effects of shape and location of micro-turbulators on unsteady shockwave-boundary layer interactions in transonic flow," *Journal of KONES*, Vol. 23, 2016.

[25] Memmolo, A., Bernardini, M., and Pirozzoli, S., "Scrutiny of buffet mechanisms in transonic flow," *International Journal of Numerical Methods for Heat & Fluid Flow*, Vol. 28, No. 5, 2018, pp. 1031–1046.

[26] Hartmann, A., Feldhusen, A., and Schröder, W., "On the interaction of shock waves and sound waves in transonic buffet flow," *Physics of Fluids*, Vol. 25, No. 2, 2013.

[27] Boussinesq, T., "Mem. pres Acad," *Sci., 3rd ed Paris*, Vol. 23, 1877, p. 46.

[28] Vreman, A., "An eddy-viscosity subgrid-scale model for turbulent shear flow: Algebraic theory and applications," *Physics of fluids*, Vol. 16, No. 10, 2004, pp. 3670–3681.

[29] Graves, R. E., and Argrow, B. M., "Bulk viscosity: past to present," *Journal of Thermophysics and Heat Transfer*, Vol. 13, No. 3, 1999, pp. 337–342.

[30] Lele, S. K., "Compact finite difference schemes with spectral-like resolution," *Journal of computational physics*, Vol. 103, No. 1, 1992, pp. 16–42.

[31] Song, H., Ghate, A. S., Matsuno, K., West, J., Subramaniam, A., Brown, L. J., and Lele, S. K., "Robust high-resolution simulations of compressible turbulent flows without filtering," *AIAA Aviation 2022 Forum*, 2022, p. 4122.

[32] Deng, X., and Zhang, H., "Developing high-order weighted compact nonlinear schemes," *Journal of Computational Physics*, Vol. 165, No. 1, 2000, pp. 22–44.

[33] Nonomura, T., Iizuka, N., and Fujii, K., "Increasing order of accuracy of weighted compact nonlinear scheme," *AIAA Paper*, Vol. 893, 2007.

[34] Zhang, S., Jiang, S., and Shu, C.-W., "Development of nonlinear weighted compact schemes with increasingly higher order accuracy," *Journal of Computational Physics*, Vol. 227, No. 15, 2008, pp. 7294–7321.

[35] Wong, M. L., and Lele, S. K., "High-order localized dissipation weighted compact nonlinear scheme for shock-and interface-capturing in compressible flows," *Journal of Computational Physics*, Vol. 339, 2017, pp. 179–209.

[36] Subramaniam, A., Wong, M. L., and Lele, S. K., "A high-order weighted compact high resolution scheme with boundary closures for compressible turbulent flows with shocks," *Journal of Computational Physics*, Vol. 397, 2019, p. 108822.

[37] Borges, R., Carmona, M., Costa, B., and Don, W. S., "An improved weighted essentially non-oscillatory scheme for hyperbolic conservation laws," *Journal of computational physics*, Vol. 227, No. 6, 2008, pp. 3191–3211.

[38] Rusanov, V. V., "The calculation of the interaction of non-stationary shock waves with barriers," *Zhurnal Vychislitel'noi Matematiki i Matematicheskoi Fiziki*, Vol. 1, No. 2, 1961, pp. 267–279.

[39] Shu, C.-W., and Osher, S., "Efficient implementation of essentially non-oscillatory shock-capturing schemes," *Journal of computational physics*, Vol. 77, No. 2, 1988, pp. 439–471.

[40] Courant, R., Friedrichs, K., and Lewy, H., "Über die partiellen Differenzengleichungen der mathematischen Physik," *Mathematische annalen*, Vol. 100, No. 1, 1928, pp. 32–74.

[41] Farin, G., *Curves and surfaces for computer-aided geometric design: a practical guide*, Elsevier, 2014.

[42] Bermejo-Moreno, I., Larsson, J., and Lele, S. K., "LES of canonical shock-turbulence interaction," *Annual Research Briefs*, 2010, pp. 209–222.

[43] Welch, P., "The use of fast Fourier transform for the estimation of power spectra: a method based on time averaging over short, modified periodograms," *IEEE Transactions on audio and electroacoustics*, Vol. 15, No. 2, 1967, pp. 70–73.

[44] Towne, A., Schmidt, O. T., and Colonius, T., "Spectral proper orthogonal decomposition and its relationship to dynamic mode decomposition and resolvent analysis," *Journal of Fluid Mechanics*, Vol. 847, 2018, pp. 821–867.

[45] Schmidt, O. T., and Colonius, T., "Guide to spectral proper orthogonal decomposition," *Aiaa journal*, Vol. 58, No. 3, 2020, pp. 1023–1033.

[46] Lumley, J. L., "The structure of inhomogeneous turbulent flows," *Atmospheric turbulence and radio wave propagation*, 1967, pp. 166–178.

[47] Lumley, J. L., "Stochastic tools in turbulence," 1970.

[48] Schmidt, O. T., Towne, A., Rigas, G., Colonius, T., and Brès, G. A., "Spectral analysis of jet turbulence," *Journal of Fluid Mechanics*, Vol. 855, 2018, pp. 953–982.

[49] Nekkanti, A., and Schmidt, O. T., "Modal analysis of acoustic directivity in turbulent jets," *AIAA journal*, Vol. 59, No. 1, 2021, pp. 228–239.

[50] Ghate, A., Towne, A., and Lele, S., "Broadband reconstruction of inhomogeneous turbulence using spectral proper orthogonal decomposition and Gabor modes," *Journal of Fluid Mechanics*, Vol. 888, 2020, p. R1.

[51] Muralidhar, S. D., Podvin, B., Mathelin, L., and Fraigneau, Y., "Spatio-temporal proper orthogonal decomposition of turbulent channel flow," *Journal of Fluid Mechanics*, Vol. 864, 2019, pp. 614–639.

[52] Souza, D. S., Rodríguez, D., Himeno, F. H., and Medeiros, M. A., "Dynamics of the large-scale structures and associated noise emission in airfoil slats," *Journal of Fluid Mechanics*, Vol. 875, 2019, pp. 1004–1034.

[53] Wong, M. L., Ghate, A. S., Stich, G.-D., Kenway, G. K., and Kiris, C. C., "Numerical study on the aerodynamics of an iced airfoil with scale-resolving simulations," *AIAA SCITECH 2023 Forum*, 2023, p. 0252.